International Journal of Medical, Medicine and Health Sciences
ISSN: 2517-9969
Vol:1, No:11, 2007

# The Role of Velocity Map Quality in Estimation of Intravascular Pressure Distribution

Ali Pashaee, Parisa Shooshtari, Gholamreza Atae and Nasser Fatouraee

***Abstract*—** Phase-Contrast MR imaging methods are widely used for measurement of blood flow velocity components. Also there are some other tools such as CT and Ultrasound for velocity map detection in intravascular studies. These data are used in deriving flow characteristics. Some clinical applications are investigated which use pressure distribution in diagnosis of intravascular disorders such as vascular stenosis. In this paper an approach to the problem of measurement of intravascular pressure field by using velocity field obtained from flow images is proposed. The method presented in this paper uses an algorithm to calculate nonlinear equations of Navier-Stokes, assuming blood as an incompressible and Newtonian fluid.

Flow images usually suffer the lack of spatial resolution. Our attempt is to consider the effect of spatial resolution on the pressure distribution estimated from this method. In order to achieve this aim, velocity map of a numerical phantom is derived at six different spatial resolutions. To determine the effects of vascular stenoses on pressure distribution, a stenotic phantom geometry is considered. A comparison between the pressure distribution obtained from the phantom and the pressure resulted from the algorithm is presented. In this regard we also compared the effects of collocated and staggered computational grids on the pressure distribution resulted from this algorithm.

***Keywords*—**Flow imaging, pressure distribution estimation, phantom, resolution.

## I. Introduction

MAGNETIC resonance Imaging (MRI) is a very versatile technique for cardiac diagnostics because of its special features. Among them, Phase-Contrast MRI can be used to measure the velocity components in the flow region [1]. This method is based on the phase difference between the transverse magnetization of blood and that of stationary tissue which are at the same location during the time of the acquisition [2]. Four dimensional phase contrast technique is also developed in [3] that permit spatial and temporal coverage of an entire three dimensional volume.

Pressure gradient is a sensitive marker for ischemia [4]. Also it has clinical value in vessel stenosis and restricted value orifice studies [5]. Simplified Bernoulli equation is commonly used in medicine to calculate the pressure differences at peak inflow over these conditions. Recently Ebbers et al [6] has developed a technique to integrate pressure gradients along specific flow streamlines computed from PC-MRI.

It has been shown that a more general relative pressure field may be calculated numerically from 2D and 3D velocity data using fluid dynamics relations [5, 7]. Both estimated pressure gradient at centerline and the distribution of pressure in flow field are obtained from velocity map. The resolution of this velocity map will affect the calculated pressure gradients.

In this paper our attempt is on studying the effect of velocity map resolution on estimation of pressure distribution derived from flow images. In this regard the Pressure-Poisson Equation (PPE) for pressure field estimation is proposed. Then an algorithm to access the pressure distribution image from PC velocity map is presented. A three dimensional model which is similar to stenosis geometry is considered for evaluation of the algorithm. Different velocity images containing various spatial resolutions are derived from this numerical phantom. Then the pressure estimation procedure is applied on these velocity maps, and the resulted pressure distribution is calculated in two computational mesh types. Finally a comparison between these methods is presented.

## II. Materials and Methods

### A. Governing Equations

The most commonly used method to obtain the pressure field from a velocity field is by first taking the divergence of the Navier-Stokes Equation. The resulted equation called Pressure-Poisson Equation (PPE) together with the Neumann boundary condition -which is the most appropriate boundary condition for PPE [8]- is expressed as,

$$\nabla^2 p = \nabla.\mathbf{b}$$
$$\nabla p.\mathbf{n} = \mathbf{b}.\mathbf{n} \quad \text{Boundary Condition} \tag{1}$$

Manuscript received November 30, 2005.

A. Pashaee is a Ph.D. student in the Biomedical Engineering Faculty, Amirkabir University of Technology (Tehran Polytechnic), Tehran, Iran (e-mail: pashaee@bme.aut.ac.ir).

P. Shooshatri, is a M.Sc. student in the Electrical Engineering Department, Sharif University, Tehran, Iran (e-mail: pshooshtari@ee.sharif.edu).

G. Atae, is with Faculty of Para Medicine, Babol University of Medical Science, Babol, Iran.

N. Fatouraee is an assistant professor in the Biomedical Engineering Faculty, Amirkabir University of Technology (Tehran Polytechnic), Tehran, Iran; P.O.Box: 15875-3413 (corresponding author, phone: +98-21-64542368; fax: +98-21-6495655; e-mail: Nasser@ aut.ac.ir).

Where $p$ is the kinematic pressure (pressure/density), $\mathbf{n}$ is the outward normal vector on surface enclosing fluid region and $\mathbf{b}$ is a function of the given velocity field $\mathbf{u}$ as below,

$$\mathbf{b} = \nu\nabla^2\mathbf{u} + \mathbf{f} - \mathbf{u}.\nabla\mathbf{u} - \frac{\partial \mathbf{u}}{\partial t} \quad (2)$$

Here $\nu$ is the kinematic viscosity and $\mathbf{f}$ is the body force per unit mass. By substituting $\mathbf{b} = \nabla p$ in (2) the Navier-Stokes equation will be obtained.

PPE is an elliptic second order partial differential equation. For this elliptic equation the pressure at a given point must be solved simultaneously with the pressure at all other points.

### B. Discretization

Different discretization techniques are used for numerical solution of Pressure-Poisson Equation. In this study we applied a Finite Difference method to calculate the pressure domain from velocity data. For deriving the velocity components and real pressure distribution in the numerical phantom, a Finite Volume technique is considered here.

Explicit discretization of PPE for three dimensional flow domain at Cartesian coordinate is generally obtained from six point central approximation as below:

$$\frac{p_{i+1,j,k} - 2p_{i,j,k} + p_{i-1,j,k}}{\Delta x_1^2} + \frac{p_{i,j+1,k} - 2p_{i,j,k} + p_{i,j-1,k}}{\Delta x_2^2} + \frac{p_{i,j,k+1} - 2p_{i,j,k} + p_{i,j,k-1}}{\Delta x_3^2} = \sum_{m=1}^{3} \frac{\partial p_{x_m}}{\partial x_m} \quad (3)$$

Where $p_{x_m} \equiv \partial p / \partial x_m$ is calculated from velocity data. Stability of this iterative method is guaranteed when it does not diverge. In practice we have found that the algorithm does converge numerically.

Finite Volume technique is used in construction of the numerical phantom. The method used in this domain is the SIMPLE (Semi-Implicit Method for Pressure Linked Equation) method [9].

### C. Estimation Procedure

The estimation of pressure distribution from flow images includes some steps. In this study the following procedure is used:

(1) Determination of the velocity field in the image and detection of the boundaries. In this study, evaluation of the estimation methods is considered, so an amenable flow domain with exact pressure distribution is needed. We used a numerical phantom to provide these data. Different spatial resolutions are considered in construction of this phantom.

(2) Construction of velocity, pressure and position data file. This file consists of information on position of grids containing data and the data on these points. Here the data file is provided from the numerical phantom.

(3) Importing these data to program, determining the maxima and minima in data file and calculating the grid dimensions. The maximum and minimum of data sets are necessary in computational cube definition. Also they are necessary in calculation of actual velocity components.

(4) Construction of computational cube. This is a three dimensional (two dimensional in 2D problems) spatial cube containing the flow domain. Minima and maxima are used to determine its dimension.

(5) Construction of data matrix. Some 4D (3D in two dimensional and steady state problems) matrix including position components, velocity components, exact and computed pressure data and masking matrix will be defined in this stage. Masking matrix isolates the fluid region from peripheral tissues.

(6) Discretization of the governing equation as discussed before.

(7) Solving the governed system of equations. In this stage we used the iterative Gauss-Seidel method to estimate the pressure domain.

## III. Experiments and Results

### A. Mathematical Phantom

In order to evaluate the effects of different spatial resolutions and its effect on computed pressure distribution, we have applied the procedure on a numerical phantom.

A three dimensional internal flow containing a high pressure gradient and a geometry which is similar to the biological conditions is considered as Fig 1. This model contains a square conduit including a sudden contraction and expansion. The geometry simulates a simple 75% area stenosis. Diameter of d=4 mm is chosen for this phantom. Flow domain of $4 \times 4 \times 80$ by step length of 2 is considered in this model. A steady state Newtonian incompressible flow is considered for this phantom. Laminar flow by Reynolds number 250 upstream of stenosis is considered for flow regime. Blood density of 1.05 g/cm$^3$ and viscosity of 3.5 centi-poise are employed in model. Two models by grid sizes of 0.1 and 0.125 mm developed in this regard. Based on the results obtained from these two models, we derived six three dimensional velocity domain images by grid sizes 0.1, 0.125, 0.2, 0.25, 0.5 and 1 mm. According to these grid sizes, the images by resolutions include 1, 2, 4, 5, 8 and 10 pixels per unit length of the geometry is obtained. Table I shows the total number of nodes and resolution for each of these phantoms.

The velocity field and gold pressure distribution of this phantom is provided via the Fluent (FLUENT 6, CFD

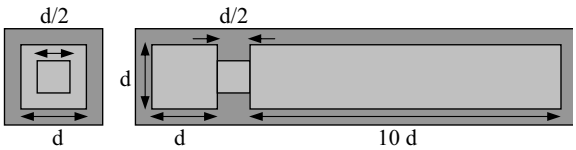


Fig. 1:Geometry of the numerical phantom. Grey region is the computational cube. The bright grey presents domain of fluid region.

software package, Fluent Inc., Lebanon, NH), which is a Finite Volume Flow Analysis Commercial Package. The velocity maps are extracted from the software and then they are used as input file in the main program. The velocity domain and pressure distribution obtained from these models is checked to correspond on each other.

In order to compare the effects of these phantoms on resulted pressure distribution, we will consider the pressure variations on centreline of this phantom.

TABLE I
INFORMATION ON GRID SIZE, RESOLUTION AND NUMBER OF DATA POINTS AT SIX NUMERICAL PHANTOMS.

| | Ph. 1 | Ph. 2 | Ph. 3 | Ph. 4 | Ph. 5 | Ph. 6 |
|---|---|---|---|---|---|---|
| Grid Sizes (mm) | 1 | 0.5 | 0.25 | 0.2 | 0.125 | 0.1 |
| Resolution n/D | 1 | 2 | 4 | 5 | 8 | 10 |
| No. of Nodes | 259 | 1533 | 10393 | 19611 | 76209 | 146221 |

### B. Convergency criterion

The criterion below is considered for diagnosis of convergency for estimation of pressure domain:

$$cr = \frac{1}{N}\left|\sum_{i=1}^{N}(\hat{p}_i^{m-1} - \hat{p}_i^{m-2})^2 - \sum_{i=1}^{N}(\hat{p}_i^{m} - \hat{p}_i^{m-1})^2\right| \le e \qquad (4)$$

Here $m$ is the iteration number, $\hat{p}$ is the estimated pressure and $N$ is the total node number at domain. In this criterion the average pressure variation at each iteration is compared by the previous one. Figure 2 presents the variations of $cr$ at various iteration numbers at 5 n/D resolution velocity field. Similar plots resulted for all phantoms. These plots show a decreasing $cr$ with iteration number. Its magnitude extends to zero, but for computational aims a very small number is the condition to stop the iterations. At this study $e = 10^{-24}$ is used for convergency condition.

Studying the convergency of different resolution phantoms, shows an increase in iteration number of convergency with increasing the resolution. Figure 3 shows the iteration number of convergency as a function of resolution. It denotes that the relation between the resolution of the image and the iteration number of convergency is not linear. Also it is obvious from this figure that the number of iteration for convergency at staggered grids is less than that of collocated computational grids. The difference between these plots is more at high resolution phantoms. Also we found that less iterations required for collocated computational grids algorithms.

### C. Error Analysis

To be assured of the resulted pressure distribution, the estimated pressure is compared with the gold pressure distribution obtained from the numerical phantoms. The comparison at different iteration numbers took place. The equation below is used for this analysis:

$$error = \frac{\sum_{i=1}^{N}(\hat{p}_i - p_i)^2}{\sum_{i=1}^{N}\hat{p}_i^2} \qquad (5)$$

Fig. 4 shows this error as a function of iteration number for typical resolution 5 n/D (5 data nodes per unit length). Here $\hat{p}_i$ is the estimated pressure and $p_i$ is the gold pressure value at node $i$ of velocity domain. This figure illustrates that after an iteration number of approximately 5000 the pressure distribution converges to a certain one. After this iteration the rate of variations is approximately zero. Solid line in this figure presents the results at Collocated computational grid and dashed line is for Staggered one.

Figure 5 shows the MSE as a function of iteration number for an image by a resolution of 5 n/D. MSE equals the mean of the squares of the deviations from target, i.e.,

$$MSE = \frac{1}{N}\sum_{i=1}^{N}(\hat{p}_i - p_i)^2 \qquad (6)$$

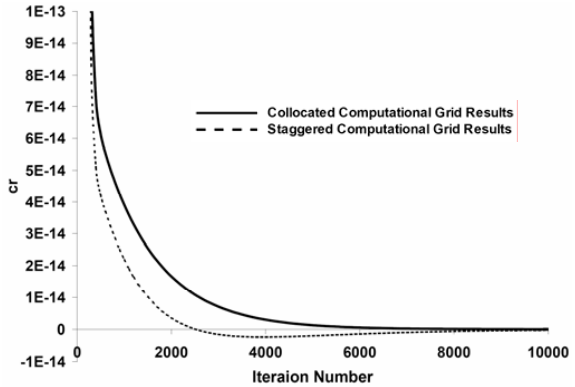


Fig. 2 $cr$ (eq. 4) as a function of iteration number. In computational algorithm the program stops when $cr$ extends to $e$.

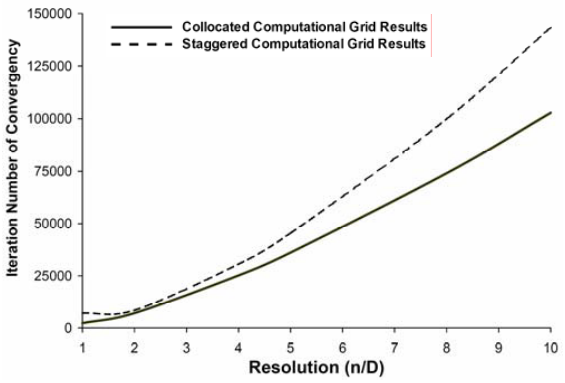


Fig. 3 The convergency iteration number at different velocity map resolutions. More iteration is needed at finer phantoms.

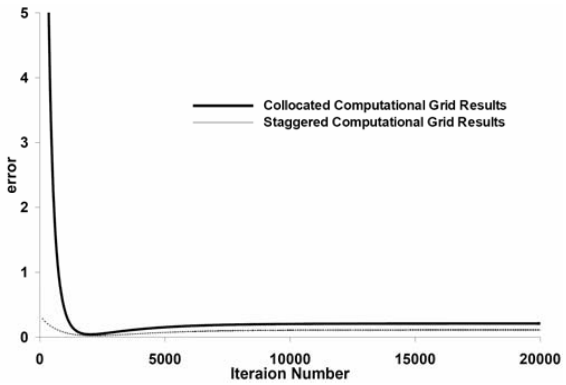


Fig. 4 Error of the resulted pressure distribution on whole data as a function of iteration number. These data is obtained from resolution 5 n/D.

According to this figure the estimated pressure gradient primarily converges to exact one and then extends to a certain distribution as the iteration number increases. The amount of error at this point is constant by variation of iterations. Detection of the iteration number for minimum MSE can lead the computations to the closest distribution to the exact one. As will be discussed later, the error for staggered computational grids is less than the collocated grids. The MSE at figure 5 is defined on all nodes of the domain, for correctness of centerline pressure gradient, it must be defined a MSE on centerline nodes.

### *D. Spatial resolution Effects*

By considering the MSE value of convergency for all of these phantoms, we found that at low resolution velocity maps, the MSE decrease with increasing the resolution, but after a certain resolution it becomes almost unchanged. Figure

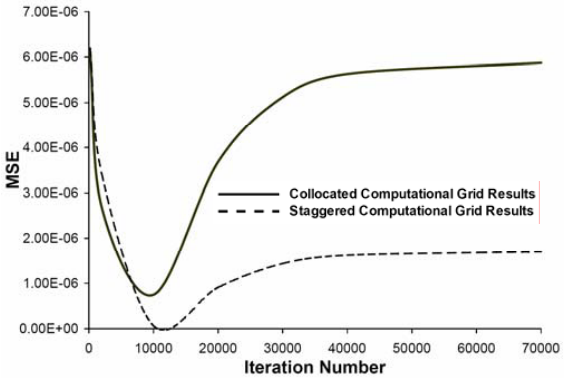


Fig. 5 Mean-Squared Error (MSE) of pressure distribution on whole data elements as a function of iteration number (phantom 10 n/D). This plot shows that MSE remains constant without any change, when the algorithm converges.

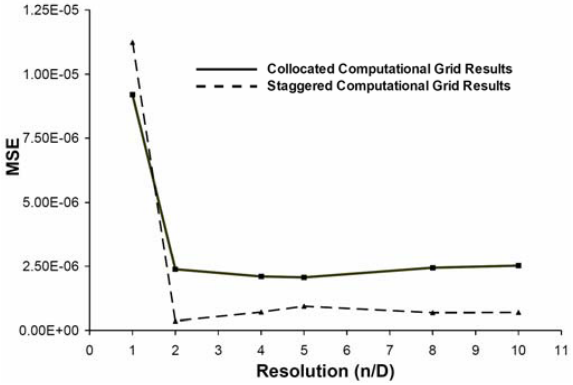


Fig. 6 The Mean-Squared Error (MSE) of pressure distribution at images with various resolutions. At resolutions more than 3 n/D a nearly constant MSE is derived.

6 shows the MSE value of convergency at different resolution images for Collocated (solid line) and Staggered (dashed line) computational grids. These results show that the MSE is approximately constant at resolutions higher than 3 n/D.

For qualitative and quantitative comparison of resolution effects, the study of pressure distribution at centerline will be sufficient. Fig 7 illustrates the pressure distribution in Collocated and staggered computational grids in resolutions of 1, 5 and 10 n/D. The general configurations of three plots are close to each other. The deviation of figure 7-a from gold pressure is due to the large grid size of this phantom. Especially this error is affected from the step region where the number of grids reduces to 1/4 initial value. Here it must be mentioned that the exact value of pressure in this figure is not so important and it is the pressure gradient that must be considered. In deriving the pressure field, its value varies by iteration. We fixed the pressure values at a certain position in each of these figures. This point is on outlet of the channel. Reviewing Fig 7 implies the importance of finer grids resolution during image acquisition. Also it is obvious that during pressure distribution estimation in small vessels the PPE algorithm only will detect the rough estimation of pressure gradients. Taking more grids during image acquisition results in a more precise pressure distribution estimation. Figure 8 shows MSE calculated from pressure gradient on centreline is obtained from these data.

### *E. Computational grid Effects*

Comparison of two Collocated (solid curve) and staggered grids (dashed curve) in figure 4 and 5 illustrates that using staggered technique results in more closer estimation of the real pressure distribution. On the other hand according to figure 3 more iteration is required for staggered grids convergency. So it is preferred to use a staggered computational grid when there is no timing considerations.

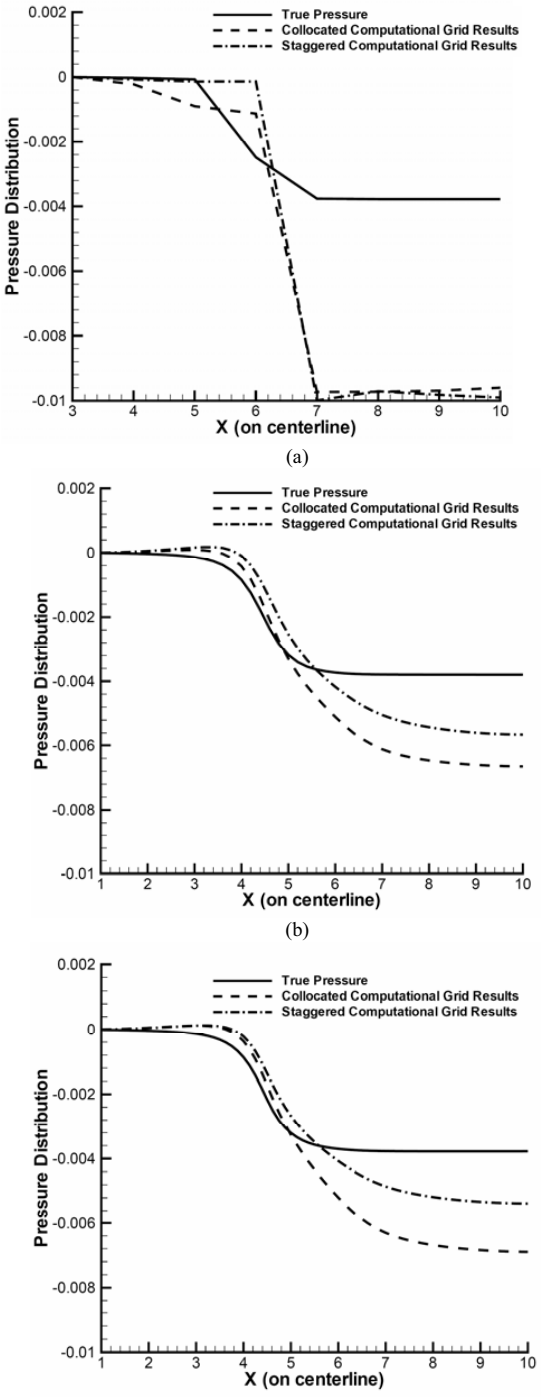


Fig. 7 Comparison of Collocated and staggered mesh Results on centerline of the phantom at resolutions (a) 1 n/D, (b) 5 n/D and (c) 10 n/D. The results compared for Collocated (dashed line) and staggered (dashed-dotted) computational grid types.

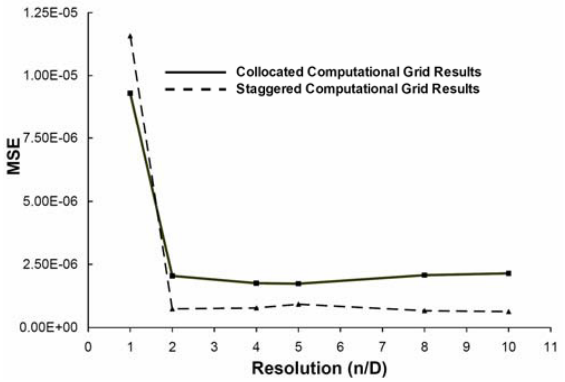


Fig. 8 The Mean-squared error for pressure gradient on centerline at various resolutions.

Figure 5 shows an approximately 6 fold error on computational grids type of collocated relative to that of staggered grids. So using the staggered computational grids may excessively decrease the errors.

Comparison of these computational techniques on different resolution images shows lower error for Collocated technique at resolution below 2 n/D (figure 6). So it is offered using the Collocated technique for very low resolutions images. According to figure 4, Staggered grids is recommended for moderate and high resolution velocity images.

## IV. Conclusion

Computation of pressure distribution estimated by numerical solution of Navier-Stokes equation using velocity map for different spatial velocity resolution is considered here. Our attempt was to know the efficiency of this method in estimation of the pressure distribution in different resolutions in vascular imaging. In this regard two computational grids considered to calculate the pressure distribution. Results show an approximately constant error for resolutions higher than 3 n/D. Figure 3 shows that the iteration number of convergency versus the resolution of images is of higher order than one, and is more for staggered computational grids than the collocated one. According to figures 6 and 8, the convergency for whole pressure distribution is similar to pressure gradient estimated at centerline. Also it is recommended using a Collocated computational grid for very low resolution velocity images and applying the Staggered one for medium and high resolutions.

## References

[1] N. Pelc, R. Herfkens, A. Shimakawa, and D. Enzmann, "Phase contrast cine magnetic resonance imaging," *Magn. Reson. Quart.*, vol. 7, no. 4, pp. 229–254, 1991.

[2] M. T. Vlaardingerbroek, and J. A. Den Boar, *Magnetic Resonance Imaging: Theory and Practice*. 3rd ed., New York: Springer Verlag, 2003.

[3] M. Markl, F. P. Chan, M. T. Alley, K. L. Wedding, M.T. Draney, C. J. Elkins, D. W. Parker, R. Wicker, C. A. Taylor, R. J. Herfkens, and N. J.

Pelc, "Time-resolved three-dimensional phase-contrast MRI," *J. Mag. Reson. Imaging*, vol. 17, pp. 499–506, 2003.

[4] N. L. Greenberg, P. M. Vandervoort, M. S. Firstenberg,M. J. Garcia, and J. D. Thomas, "Estimation of diastolic intraventricular pressure gradients by Doppler M-mode echocardiography," *Am. J. Physiol. Heart Circ. Physiol.*, vol. 280, pp. H2507-H2515, 2001.

[5] J. M. Tyszka, D. H. Laidlaw, J. W. Asa, and J. M. Silverman, "Three-Dimensional, Time-Resolved (4D) Relative Pressure Mapping Using Magnetic Resonance Imaging," *Journal of Magnetic Resonance Imaging*, vol. 12, pp. 321-329, 2000.

[6] T. Ebbers, L. Wigstrom, A. Bolger, J. Engvall, and M. Karlsson, "estimation of relative cardiovascular pressures using time-resolved three-dimensional phase-contrast MRI," *Magnetic Resonance Imaging*, vol. 45, pp. 872-879, 2001.

[7] G. Z. Yang, P. J. Kilner, N. B. Wood, S. R. Underwood, and D. N. Firmin, "Computation of flow pressure fields from magnetic resonance velocity mapping," *Magnetic Resonance Imaging*, vol. 36, pp. 520-526, 1996.

[8] S. M. Song, R. M. Leahy, D. P. Boyd, B. H. Brundage, and S. Napel, "Determining cardiac velocity fields and intraventricular pressure distribution from a sequence of Ultrafast CT cardiac images," *IEEE Trans. Med. Imaging*, vol. 13, no. 2, pp. 386-397, 1994.

[9] J. H. Ferziger, and M. Peric, *Computational methods for fluid dynamics.* 3rd ed., New York: Springer-Verlag, 2002.

[10] A. Nasiraei-Moghaddam, G. Behrens, N. Fatouraee, R. Agarwal, E. T. Choi, and A. A. Amini, "Factors affecting the accuracy of pressure measurements in vascular stenoses from phase-contrast MRI," *Magnetic Resonance in Medicine*, vol. 52, pp. 300–309, 2004.